Multiphase identification in Ni–PbTe contacts by EBSD and aberration-corrected STEM

FERRERES, Xavier Reales, CASILLAS, Gilberto, AMINORROAYA-YAMINI, Sima and GAZDER, Azdiar A.

Materials & Design 185 (2020) 108252

Contents lists available at ScienceDirect

Materials & Design

journal homepage: www.elsevier.com/locate/matdes

Multiphase identification in Ni–PbTe contacts by EBSD and aberration-corrected STEM

Xavier Reales Ferreres [a,*], Gilberto Casillas [b], Sima Aminorroaya-Yamini [c], Azdiar A. Gazder [b]

[a] Institute of Superconducting and Electronic Materials, University of Wollongong, New South Wales, 2500, Australia
[b] Electron Microscopy Centre, University of Wollongong, New South Wales, 2500, Australia
[c] Department of Engineering and Mathematics, Sheffield Hallam University, Sheffield S1 1WB, United Kingdom

HIGHLIGHTS

- The rapid SPS fabrication technique produces a two-phase monoclinic Ni_3Te_2 & orthorhombic $Ni_{2.88}Te_2$ interlayer.
- Orthorhombic to monoclinic phase transition is smooth as unit cell differences are small & 2 previously unknown ORs prevail.
- Ordered Ni vacancies in (200) planes of monoclinic Ni_3Te_2 caused the variation in intensity seen in the HAADF images.

GRAPHICAL ABSTRACT

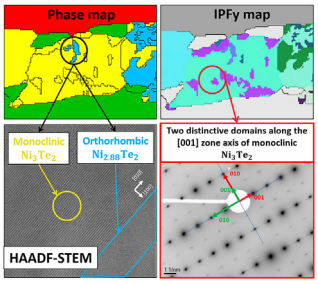

ARTICLE INFO

Article history:
Received 13 May 2019
Received in revised form
28 August 2019
Accepted 3 October 2019
Available online 10 October 2019

Keywords:
NiTe
Electron back-scattering diffraction (EBSD)
Orientation relationships
High angle annular darkfield
Scanning transmission microscopy (HAADF-STEM)

ABSTRACT

EBSD in combination with aberration-corrected STEM is used to study the interfacial layer forming at Ni electrode - PbTe thermoelectric material interfaces. Contrary to previous studies, both orthorhombic and monoclinic phases are identified within the interfacial layer. EBSD and STEM data at interphase boundaries demonstrate an approximately smooth transition from orthorhombic to monoclinic phase with almost no crystal defects due to the small differences in lattice parameters and the prevalence of one of two previously unknown orientation relationships between the phases. Moreover, the presence of special boundaries resulting in orientation domains within both phases throughout the interfacial nickel telluride layer needs to be considered when fabricating future thermoelectric devices.

1. Introduction

A nickel metal electrode bonded to a high efficient lead telluride (PbTe) thermoelectric material, results in the formation of a <20 μm thick interfacial diffusion barrier layer comprising a binary compound of nickel telluride which is suitable for the fabrication of thermoelectric modules [1,2]. In order to have a better understanding of the long-term chemical stability and electronic transport properties of the PbTe–Ni bond for thermoelectric devices, the crystallographic identification of the interfacial nickel telluride phase is important; especially since a wide range of compositions are possible.

Binary nickel telluride compounds comprise three nominal phases namely, Ni-rich β (β_1, β_1' and β_2), intermediate γ (γ_1 and γ_2),

* Corresponding author.
E-mail address: xrf042@uowmail.edu.au (X.R. Ferreres).

https://doi.org/10.1016/j.matdes.2019.108252

and Te-rich δ [3,4]. The high temperature β_1 phase (fcc) extends from 37 at.% Te (at 1004.5 °C) to 43.5 at.% Te (880 °C) [5]. Below 793 °C, the β_1 phase transforms to $\beta_1^{'}$ (fcc). At 37.7 at.% Te and 731 °C, the $\beta_1^{'}$ phase undergoes a eutectoid transition to Ni and β_2. Alternatively, at temperatures below 790 °C, the $\beta_1+\beta_1^{'}$ phases transform to β_2; with the latter phase having maximum widths extending from 38.8 at.% Te (731 °C) to 41 at.% Te (775 °C). Consequently, at room temperature, the β_2 phase is considered broadly homogeneous and stable and exists between metallic Ni ($\leq$38.8 at.% Te) and $NiTe_{0.9}$ compound ($\geq$41 at.% Te) [5,6].

In this study we focus on the β_2 phase whose chemical composition is nominally referred to as $Ni_{3\pm x}Te_2$ and is reported to possess crystal structures similar to defective/metal deficient Cu_2Sb-type (space group 129, $P4/nmm$) [5,11] or Rickardite −type ($Cu_{4-x}Te_2$, [3]) structures. The β_2 phase transforms from a tetragonal crystal structure (space group 129, $P4/nmm$) at high temperatures (~790-337 °C) through an orthorhombic crystal structure (space group 59, $Pmmn$) at intermediate temperatures (337-218 °C) into a monoclinic crystal structure (space group 11, $P2_1/m$) between ~218 °C and room temperature [7]. Previous X-ray diffraction studies [3,6] have also reported a possible disorder-order transition of β_2 phase from high temperature tetragonal crystal structure to room temperature monoclinic and tetragonal superstructures. In this regard, a study on Rickardite-type $Cu_{2.8}Te_2$ [8] was cited [3] to provide the justification for this transition. Similar intensity ratios of the crystal structures in the β_2 and $Cu_{2.8}Te_2$ phases led authors to conclude that the interstitial Ni(II) atoms in the β_2 phase were similar to the random distribution of the extra 0.8 Cu atoms over equivalent positions in the $Cu_{2.8}Te_2$ unit cell. Consequently, the interstitial Ni(II) atoms in the β_2 phase were associated with the disorder-order transition from high to room temperature.

However, Stevels [9] and Kok et al. [6] showed that upon slow cooling from 577 °C to room temperature (presumably undertaken in a furnace), the high temperature tetragonal $Ni_{2.86}Te_2$ (space group 129, $P4/nmm$) transforms to either, room temperature monoclinic Ni_3Te_2 (space group 11, $P2_1/m$) or tetragonal $Ni_{2.86}Te_2$ (space group 115, $P\bar{4}m2$). The latter two phases possess *a*-axes that are double that of the high temperature tetragonal crystal system.

Further theoretical analysis [9] using Landau theory [10] showed that second-order transformations from a high temperature tetragonal crystal structure to room temperature monoclinic and/or tetragonal crystal structures were not possible without the formation of an intermediate orthorhombic phase (space group 59, $Pmmn$). This is supported by experimental results [6], confirming the formation of an intermediate orthorhombic phase between 247 °C and 77 °C for transition from a high temperature tetragonal crystal structure to room temperature Ni_3Te_2 monoclinic or $Ni_{2.86}Te_2$ tetragonal crystal structures. Upon quenching from 330 °C, a room temperature orthorhombic phase was found to coexist with the monoclinic crystal structure; instead of the room temperature tetragonal crystal structure [6].

To-date, the crystal structures of the room temperature β_2 phase are still under debate as all phases and correlated crystal structures of nickel telluride were ascertained from X-ray diffraction studies on powder samples [3,6] or by energy dispersive X-ray spectroscopy (EDS) in a scanning electron microscope [1]. Both methodologies are significantly limited in providing accurate phase identification. Since the phases tend to form in small volume fractions in-between Ni electrodes and PbTe thermoelectric materials, the X-ray diffraction signal is highly limited. Alternatively, EDS is limited in precisely quantifying and discriminating small differences in chemical composition.

The design and production of thermo-electric materials and their devices is the subject of current and ongoing research around the world; as this directly affects how they are subsequently analysed. For example − in this study, nickel telluride is an interlayer − which means the interface between nickel and thermoelectric PbTe cannot be analysed by conventional XRD. Moreover, the phases within nickel telluride are too similar in chemical composition to be discriminated accurately by EDS. Consequently, this study provides an alternate means to quantify and characterise such phases when faced with such issues.

Here, we study the nickel telluride interfacial layer using the electron back-scattering diffraction (EBSD) technique to discriminate phases [11]. In brief, this technique returns the crystallographic orientation of a phase when the Kikuchi bands in the experimental electron back-scattering pattern (EBSP) is close to the simulated Kikuchi band of a reference crystal [12,13]. The degree of misfit between the experimental and simulated EBSPs is expressed as the mean angular deviation.

Since the accuracy of EBSD relies on prior knowledge of a phase's existence, we also employed aberration-corrected high-angle annular darkfield (HAADF) - scanning transmission electron microscopy (STEM) to directly evidence the phases in the interfacial nickel telluride layer. Due to the high spatial resolution of HAADF-STEM, it is possible to identify and visually confirm phase changes from one unit cell to the next. In doing so, we find that the nickel telluride interfacial diffusion barrier layer consists of both orthorhombic and monoclinic β_2 phases.

2. Experimental and analytical procedure

High purity Ni plate (99.99%) supplied by Advent Research Materials was bonded to a sintered PbTe pellet using a rapid fabrication spark plasma sintering (SPS) method. The SPS system comprises a vacuum chamber and vertically placed stainless steel electrodes; both of which are connected to an external water circulation system. A Ni plate and pre-sintered PbTe pellet are placed in-between graphite spacers, with the stainless steel electrodes subjecting the entire assembly to compression at 20 MPa. The interfacial β_2 phase forms between the Ni plate and a pre-sintered PbTe pellet at temperatures up to 520 °C. Following this, room temperature water circulates through the chamber walls and electrodes to rapidly cool the pellet down at ~2 °C/s via a combination of radiative and conductive cooling [14]. Further details including fabrication methods and identification of phases are provided in Refs. [14,15]. The sintered pellets were cross-sectioned, mounted in conductive resin, automatically polished up to the 1 μm diamond stage and Ar ion milled at 1 kV for 20 h on a Leica TIC-020 cross-sectional ion mill.

Simultaneous EDS and EBSD was undertaken on a JEOL JSM-7001F field emission gun-scanning electron microscope operating at 15 kV, ~6.5 nA probe current, 12 mm working distance, and 1500 × magnification fitted with an Oxford Instruments (OI) Nordlys-II(S) camera interfacing with the AZtec acquisition software suite. A step size of 0.06 μm was employed such that a map comprising 1150 × 225 pixels was collected over 2.08 h corresponding to an area of 69 × 13.5 μm^2.

EDS maps were obtained using a 20 keV energy range, 2048 channels, a process time of 2, a detector dead time of 50−55% and a pixel dwell time of 13.4 ms. Over the full 'TruMap' area, the Ni−K, Te-L and Pb-M lines returned a distribution of relative frequency versus counts per second (cps) with maximum counts of 688, 967, 1406, respectively.

The cards to index the EBSPs of the Ni, monoclinic Ni_3Te_2, tetragonal $Ni_{2.86}Te_2$, orthorhombic $Ni_{2.88}Te_2$ and PbTe phases were produced from *.CIF files downloaded from the International Crystal Structure Database (ICSD) server and converted to *.CRY files suitable for input into the OI Aztec software suite (Tables 1–3).

At each pixel, the image of the EBSP was saved upon acquisition at an exposure time of ~12 ms at 34.7 Hz using 4 × 4 binning and one background frame. Subsequent post-processing involved

Table 1
Description of Ni_3Te_2 monoclinic crystal structure, detailing space group (number, name), lattice parameters, and structure parameters (atom type, descriptor, spatial position (x, y, z), occupancy, Wyckoff position, symmetry).

Space group	Lattice parameters						Structure parameters							
(No., Name)	a	b	c	α	β	γ	Atom	Descr.	x	y	z	Occ.	Wp	Sym.
11, $P2_1/m$	7.5382	3.7934	6.0883	90.000	91.159	90.000	Ni	Ni1	0.6330	0.2500	0.2980	1.00	2e	m
							Ni	Ni2	0.3730	0.2500	0.0070	1.00	2e	m
							Ni	Ni3	0.8730	0.2500	0.9920	1.00	2e	m
							Te	Te1	0.1181	0.2500	0.7158	1.00	2e	m
							Te	Te2	0.6212	0.2500	0.7126	1.00	2e	m

Table 2
Description of $Ni_{2.86}Te_2$ tetragonal crystal structure with origin 2 detailing space group (number, name), lattice parameters, and structure parameters (atom type, descriptor, spatial position (x, y, z), occupancy, Wyckoff position, symmetry).

Or.	Space group	Lattice parameters						Structure parameters							
	(No., Name)	a	b	c	α	β	γ	Atom	Descr.	x	y	z	Occ.	Wp	Sym.
2	129, P4/nmm	3.7820	3.7820	6.0620	90.000	90.000	90.000	Ni	Ni1	−0.2500	0.2500	0.0000	1.00	2a	-4m2
								Ni	Ni2	−0.2500	0.7500	0.6900	1.00	2c	4 mm
								Te	Te1	−0.2500	0.7500	0.2900	1.00	2c	4 mm

Table 3
Description of $Ni_{2.88}Te_2$ orthorhombic crystal structure with origin 2, detailing space group (number, name), lattice parameters, and structure parameters (atom type, descriptor, spatial position (x, y, z), occupancy, Wyckoff position, symmetry).

Or.	Space group	Lattice parameters						Structure parameters						
	(No., Name)	a	b	c	α	β	γ	Atom	Descr.	x	y	z	Occ.	Wp
2	28, Pma2	7.5382	3.7879	6.0647	90.000	90.000	90.000	Ni	Ni1	0.0000	0.0000	0.2980	1.00	2a
								Ni	Ni2	0.2500	0.5000	0.68900	1.00	2c
								Ni	Ni3	0.0000	0.5000	0.0000	1.00	2b
								Ni	Ni4	0.2500	0.0330	0.0020	1.00	2c
								Te	Te1	0.0000	0.0000	0.7218	1.00	2a
								Te	Te2	0.2500	0.5000	0.2951	1.00	2c

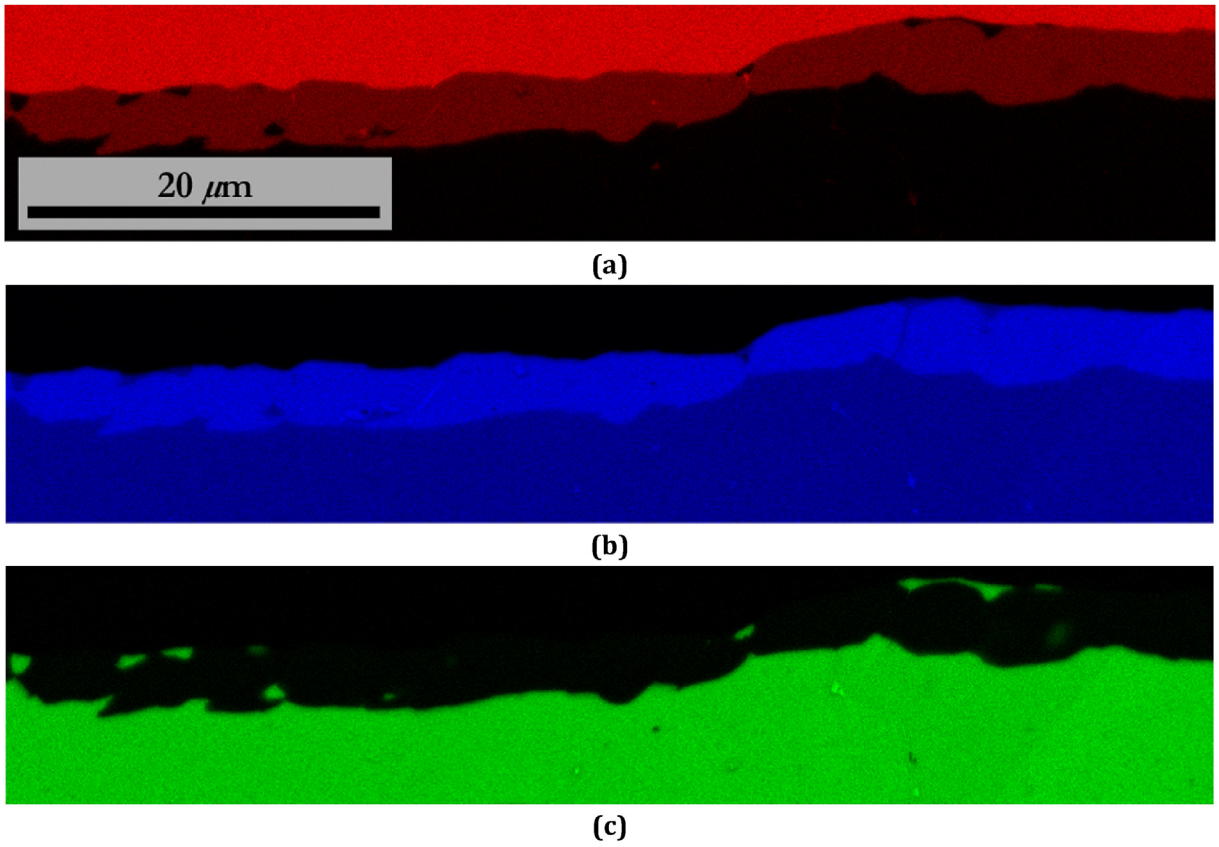

Fig. 1. (a) Energy dispersive X-ray spectroscopy maps of (a) Ni–K (red), (b) Te-L (blue) (c) Pb-M (green).

indexing of up to 11 Kikuchi bands at a constant Hough resolution of 60 via the OI "Refined Accuracy" algorithm.[1] A default number of 44 and 40 reflectors were used for Ni and PbTe, respectively. A default number of 44, 43 and 42 reflectors were used for monoclinic Ni_3Te_2, orthorhombic $Ni_{2.88}Te_2$ and tetragonal $Ni_{2.86}Te_2$, respectively.

Post-processing of the EBSD maps was undertaken using the Oxford Instruments (OI) Channel-5 software suite. In brief, it involved the removal of wild spikes and cyclic extrapolation of zero solutions up to five neighbours followed by thresholding the band contrast to delineate the unindexed regions. Following this, the maps were exported as Channel Text Files (*.CTFs) for subsequent characterisation in MATLAB and the MTEX toolbox [16,17].

In all maps, misorientations (θ) between 2° and 15° are defined as low-angle boundaries whereas $\theta \geq 15°$ denote high-angle boundaries. Special boundaries are defined using their preferential angle-axis relationship with an angular deviation $(\delta) = \pm 5°$. Where relevant, the equivalent circle diameter of subgrains and grains are calculated using critical misorientation angles of 2° and 15°, respectively; with boundary completions allowed down to 2° for both calculations.

Focused ion beam lamellae were cut from individuals grains comprising the interfacial nickel telluride layer using an FEI Helios Nanolab G3 CX FIB-SEM. Atomic resolution HAADF STEM micrographs were acquired on a probe-corrected, cold field emission gun JEOL JEM-ARM200F with 68 and 180 mrad inner and outer collection angles, respectively.

3. Results and discussion

Prior EDS of the interfacial nickel telluride layer did not find any chemical inhomogeneities in the interfacial nickel telluride layer (Fig. 1) and suggested the formation of an intermetallic compound with the chemical formula $Ni_{3\pm x}Te_2$ [1,14]. Since previous studies

[1] This algorithm provides greater accuracy in orientation determination by accounting for the parabolic shape of individual Kikuchi bands in an EBSP.

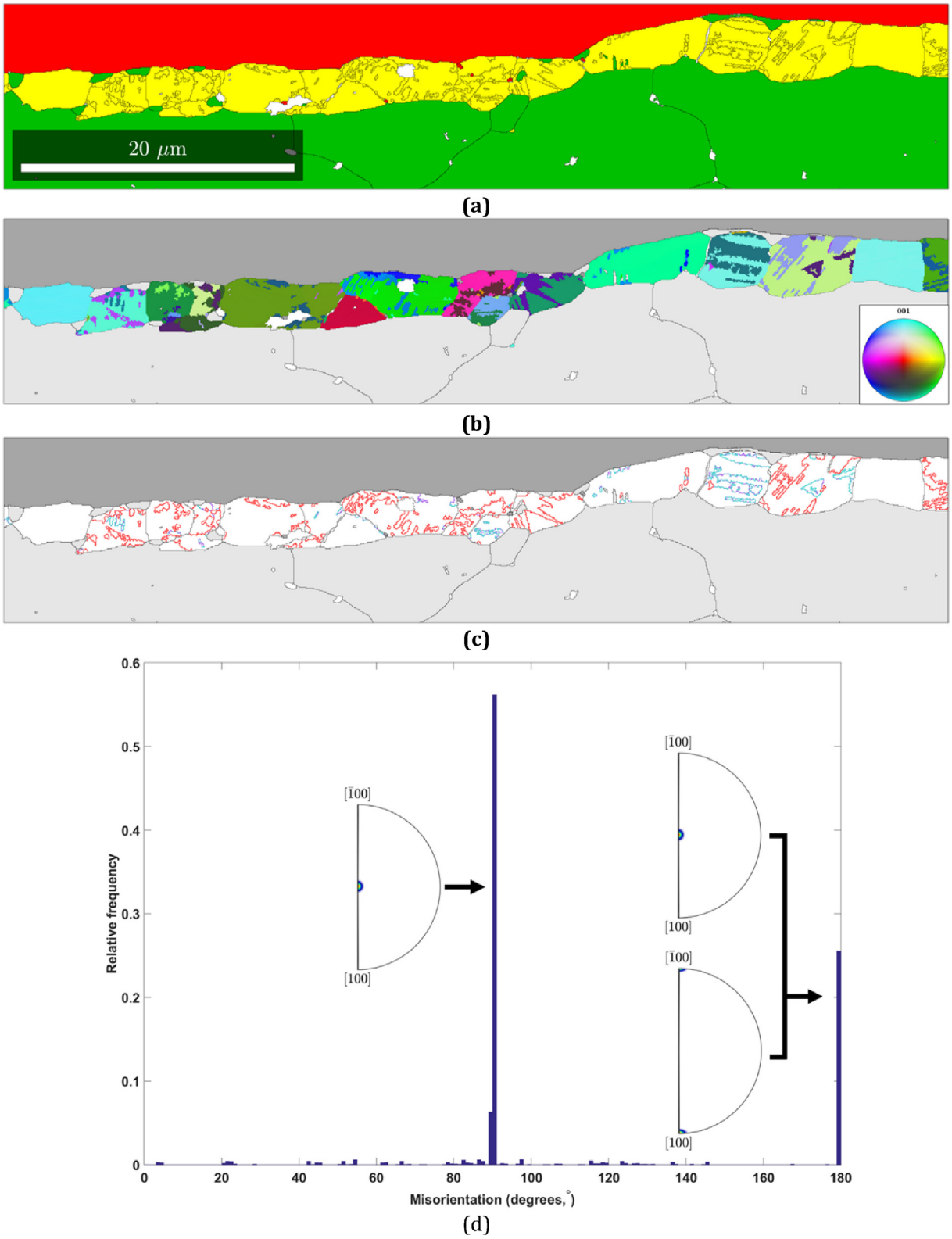

Fig. 2. (a) Phase map of Ni (red), monoclinic Ni_3Te_2 (yellow) and PbTe (green). (b) Inverse pole figure (IPF) map along the map vertical direction of monoclinic Ni_3Te_2. (c) Boundary map and (d) histogram of relative frequency versus misorientation angle, of monoclinic Ni_3Te_2 showing angle/axes corresponding to 90°[001] (red), 180°[001] (purple) and 180°[100] (teal). In (a) and (b) white = zero solutions.

[6,9] suggest a stable, room temperature monoclinic Ni_3Te_2 phase, we employed monoclinic Ni_3Te_2 (Table 1) to initially index the interfacial nickel telluride layer in the EBSD map.

Fig. 2a is the phase map with defects (cracks and holes) within the interfacial Ni–Te clearly visible in white. The top Ni, bottom PbTe and interlayer monoclinic Ni_3Te_2 phases are shown in red, green and yellow, respectively. The inverse pole Figure (IPF) map of monoclinic Ni_3Te_2 is plotted in Fig. 2b based on their crystal

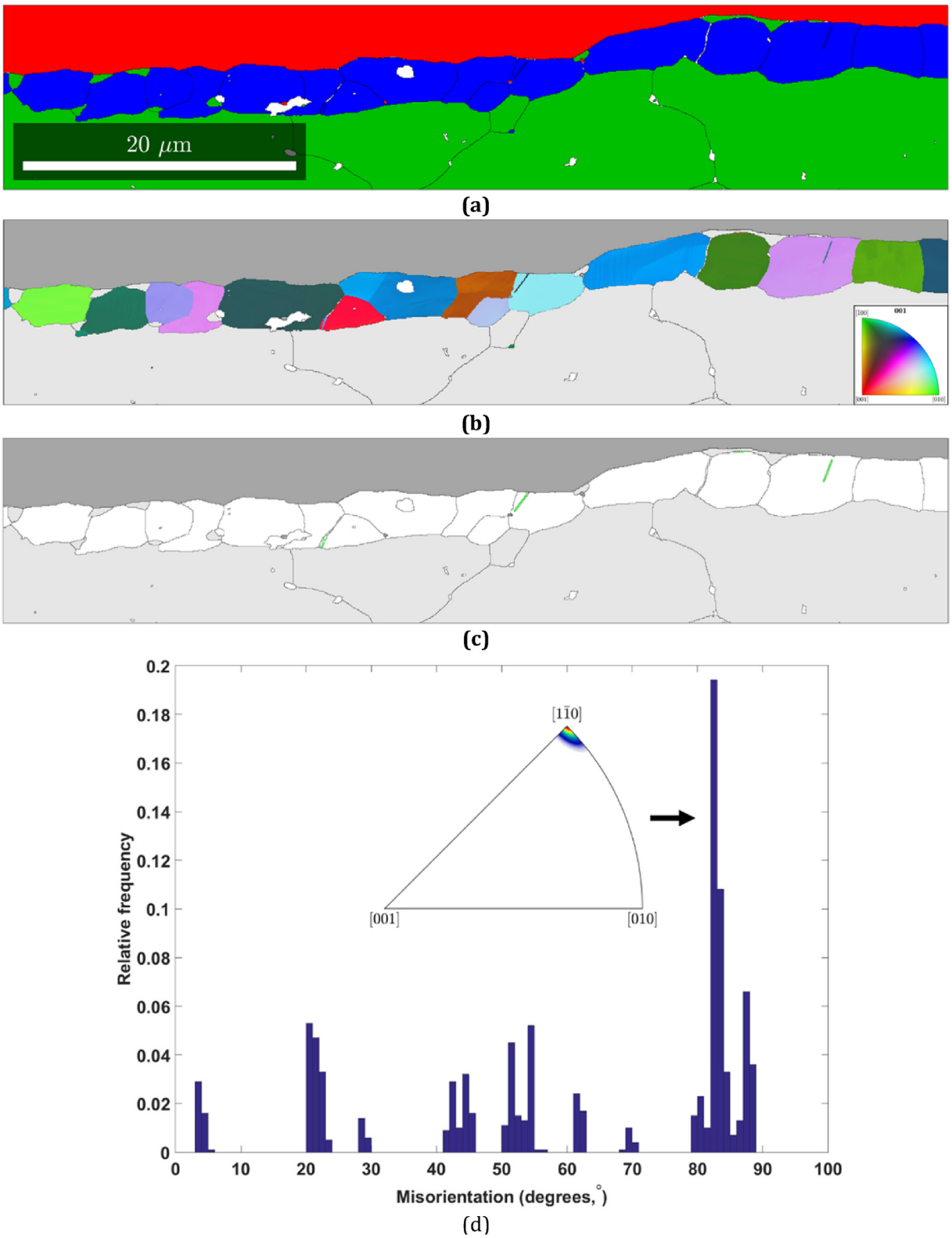

Fig. 3. (a) Phase map of Ni (red), tetragonal $Ni_{2.86}Te_2$ (dark blue) and PbTe (green). (b) Inverse pole figure (IPF) map along the map vertical direction of tetragonal $Ni_{2.86}Te_2$. (c) Boundary map and (d) histogram of relative frequency versus misorientation angle, of tetragonal $Ni_{2.86}Te_2$ showing angle/axes corresponding to $\sim 82^{\circ}$ [1$\bar{1}$0] (green). In (a) and (b) white = zero solutions.

symmetry groups along the map vertical direction, which is parallel to the macroscopic compression axis. It is apparent that within indexed grains, discrete orientation domains are visible. Here a discrete orientation domain refers to a localised area within a grain where a group of pixels are indexed with a particular orientation. It follows that within any one grain, orientation domains exist with specific misorientation angles/axes between them. Fig. 2c shows that the misorientation angles/axes between discrete orientation

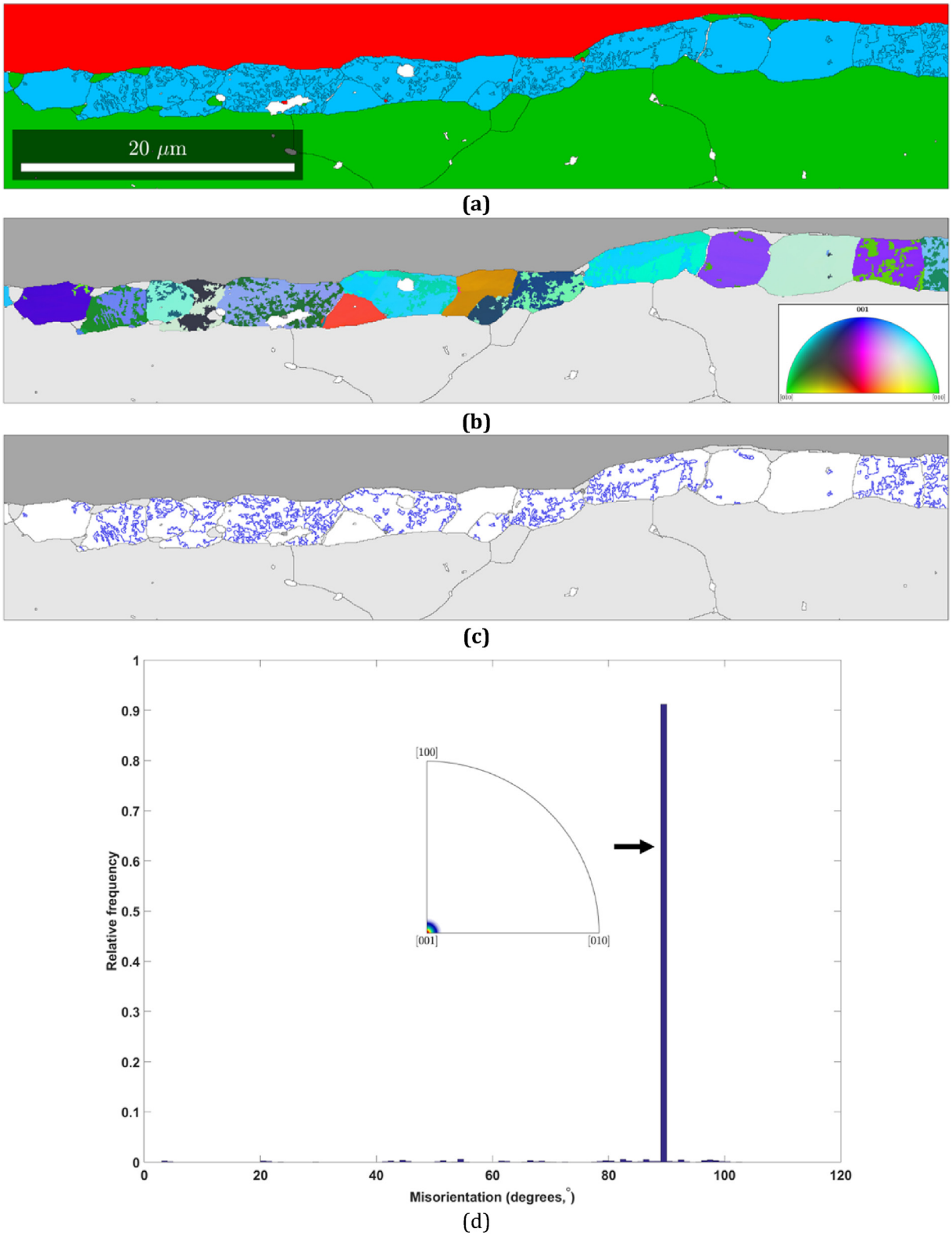

Fig. 4. (a) Phase map of Ni (red), orthorhombic $Ni_{2.88}Te_2$ (light blue) and PbTe (green). (b) Inverse pole figure (IPF) map along the map vertical direction of orthorhombic $Ni_{2.88}Te_2$. (c) Boundary map and (d) histogram of relative frequency versus misorientation angle, of orthorhombic $Ni_{2.88}Te_2$ showing angle/axes corresponding to 90°[001] (blue). In (a) and (b) white = zero solutions.

domains correspond to 90°[001] (red), 180°[001] (purple) and 180°[100] (teal). In an orientation microscopy sense, the presence of localised regions within individual grains comprising two or more distinct orientations delineated by specific angle/axis relationships are symptomatic of pseudosymmetry or discrete orientation domains of a superlattice structure (Fig. 2b and c).

Alternatively, the presence of discrete orientation domains within monoclinic Ni_3Te_2 grains suggests that a secondary phase

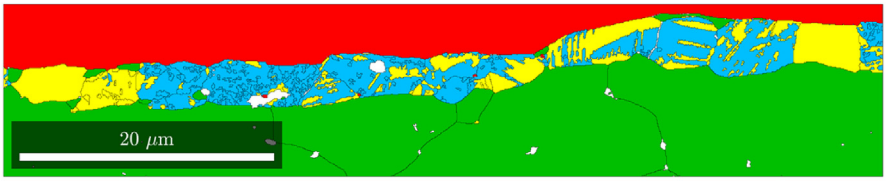

(a)

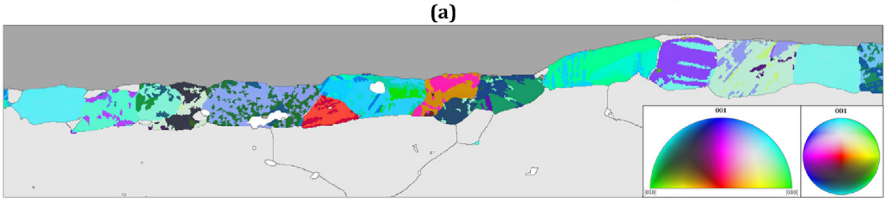

(b)

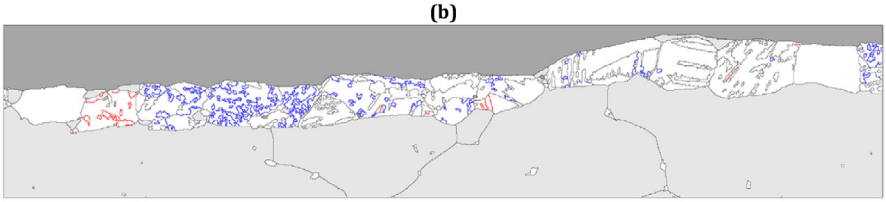

(c)

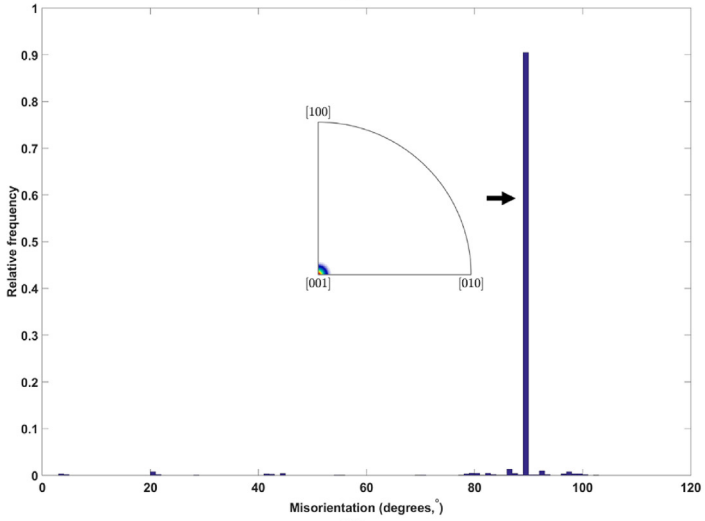

(d)

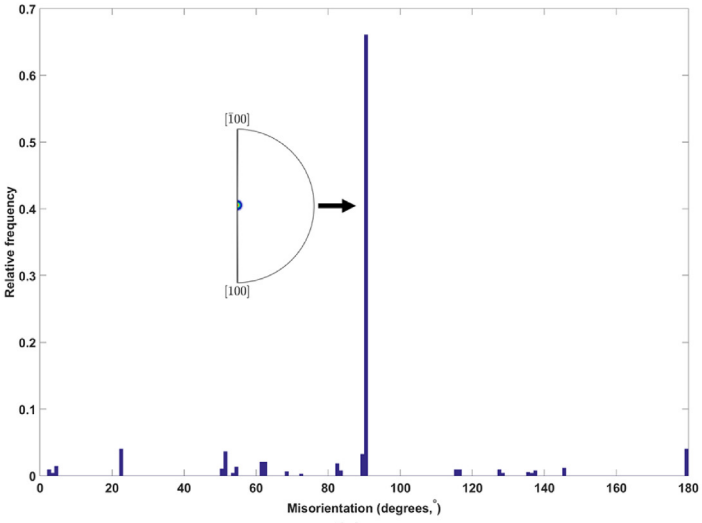

(e)

Fig. 5. (a) Phase map of Ni (red), orthorhombic $Ni_{2.88}Te_2$ (light blue), monoclinic Ni_3Te_2 (yellow) and PbTe (green). (b) Inverse pole figure (IPF) map along the map vertical direction of orthorhombic $Ni_{2.88}Te_2$ and monoclinic Ni_3Te_2. (c) Boundary map and (d, e) histograms of relative frequency versus misorientation angle, of (d) orthorhombic $Ni_{2.88}Te_2$ showing angle/axes corresponding to 90° [001] (blue) and (e) monoclinic Ni_3Te_2 showing angle/axes corresponding to 90° [001] (red). In (a) and (b) white = zero solutions.

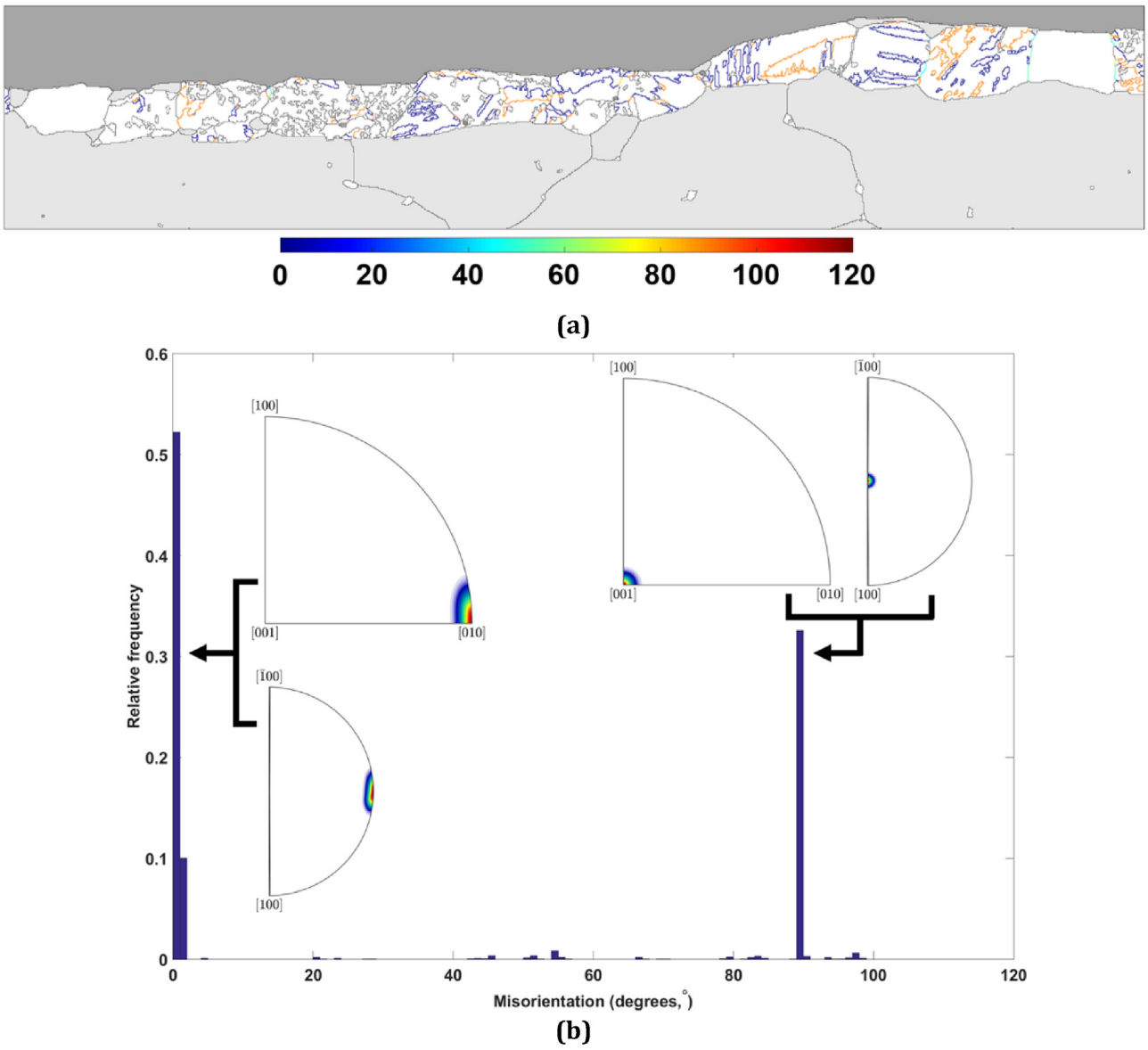

Fig. 6. (a) Interphase boundary map of orthorhombic $Ni_{2.88}Te_2$ and monoclinic Ni_3Te_2. (b) Histogram of relative frequency versus misorientation angle between orthorhombic $Ni_{2.88}Te_2$ and monoclinic Ni_3Te_2 showing preferential orientation relationships. Orientation relationship 1 (b, left) is $(010)_{ortho}$ || $(010)_{mono}$, $[001]_{ortho}$ || $[001]_{mono}$ with an ideal misorientation angle of 1.16° and ideal axes $[010]_{ortho}$ || $[010]_{mono}$. Orientation relationship 2 (b, right) is $(010)_{ortho}$ || $(100)_{mono}$, $[001]_{ortho}$ || $[001]_{mono}$ with an ideal misorientation angle of 90.0059° and ideal axes $[001]_{ortho}$ || $[001]_{mono}$.

may also be present. In this regard, the secondary phase may comprise the remnant high-temperature, tetragonal $Ni_{2.86}Te_2$ or the transitional, orthorhombic $Ni_{2.88}Te_2$ crystal structures. The tetragonal and orthorhombic phases are similar in terms of their lattice parameters on account of atomic position differences of ~0.01 nm or less [18]. Consequently, the interfacial nickel telluride layer in the EBSD map was re-indexed using both these crystal structures consecutively.

In Figs. 3a and 4a, the phase maps of the top Ni and bottom PbTe are shown in red and green, respectively. The interlayer tetragonal $Ni_{2.86}Te_2$ and orthorhombic $Ni_{2.88}Te_2$ phases are shown in Figs. 3a and 4a in dark and light blue, respectively. IPF maps of the tetragonal $Ni_{2.86}Te_2$ and orthorhombic $Ni_{2.88}Te_2$ phases are plotted in Figs. 3b and 4b based on their crystal symmetry groups along the map vertical direction, which is parallel to the macroscopic compression axis. It is immediately apparent that when the interfacial nickel telluride layer is indexed as tetragonal $Ni_{2.86}Te_2$ (Fig. 3b), discrete orientation domains are absent; as each grain corresponds to a particular orientation. The only special boundaries correspond to twin-like structures (in green in Fig. 3c) with misorientation angles/axes corresponding to $\sim 82^{\circ}[1\bar{1}0]$ (Fig. 3c and d). On the other hand, when the same plots are created for the orthorhombic $Ni_{2.88}Te_2$ phase (Fig. 4b and c), discrete orientation domains with angle/axes corresponding to $90^{\circ}[001]$ (blue) are observed.

Since it is unlikely that the thermodynamically unstable, high-temperature tetragonal $Ni_{2.86}Te_2$ crystal structure is present at room temperature, it is more probable then that the interfacial nickel telluride layer comprises both, the room-temperature, monoclinic Ni_3Te_2 and the transition $Ni_{2.88}Te_2$ orthorhombic crystal structures; with both phases making up the discrete orientation domains within each grain. This hypothesis is checked by re-indexing the EBSD map of the interfacial nickel telluride layer using both these crystal structures simultaneously.

The phase and IPF maps of the interfacial nickel telluride layer re-indexed using both, monoclinic Ni_3Te_2 and orthorhombic

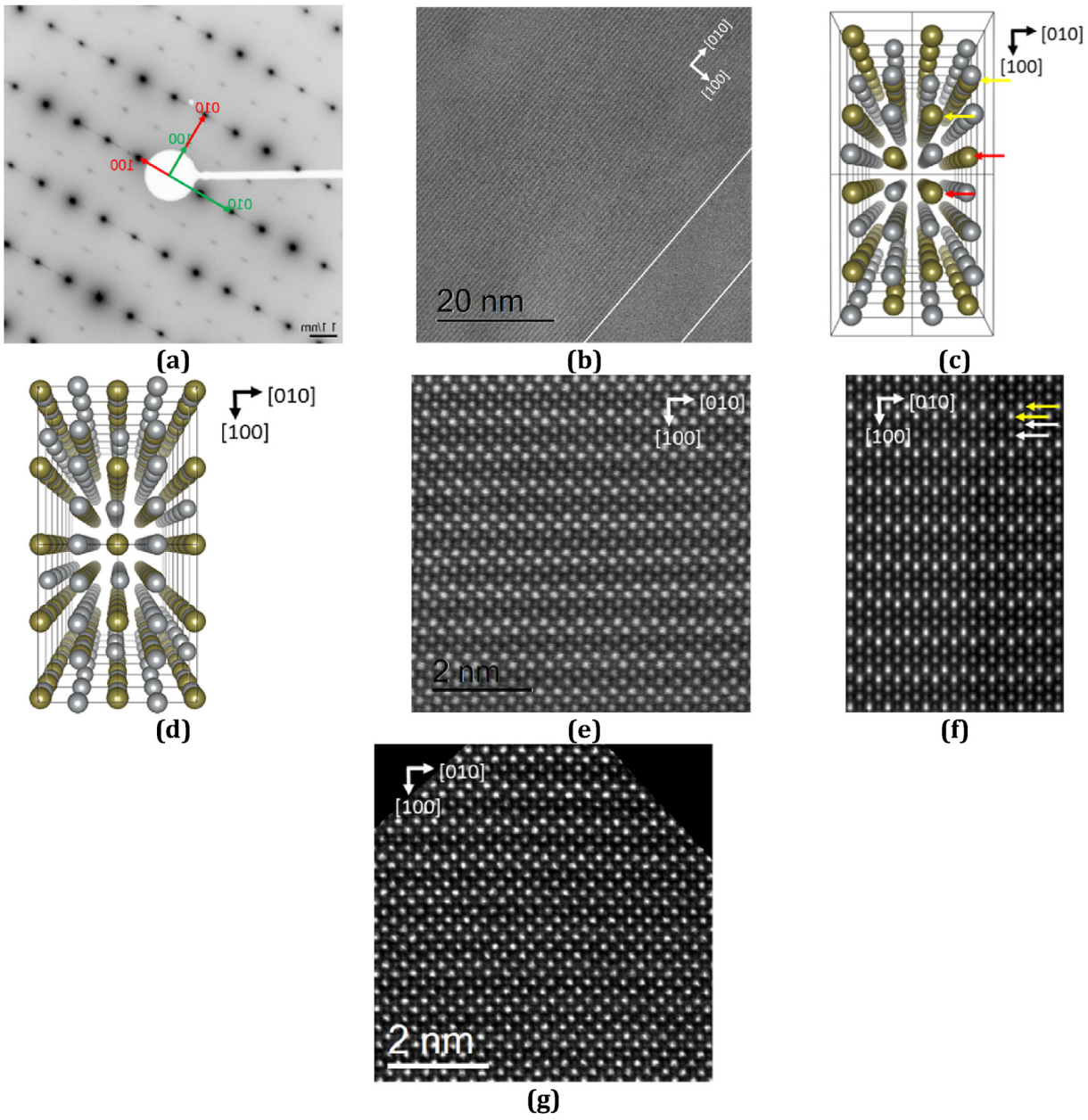

Fig. 7. (a) Selected area diffraction pattern of a monoclinic Ni_3Te_2 grain along the $[001]_{mono}$ zone axis. The strong and weak reflections belong to two monoclinic domains, denoted by the green and red arrows, present in the same area from where the diffraction pattern was collected. (b) Atomic resolution HAADF-STEM image showing most planes with modulated intensities comprising monoclinic Ni_3Te_2. In (b), the planes in the region in-between the white lines at the bottom right-hand side have no modulation in intensity and comprise orthorhombic $Ni_{2.88}Te_2$. $2 \times 2 \times 7$ supercells of (c) monoclinic Ni_3Te_2 and (d) orthorhombic $Ni_{2.88}Te_2$ along the $[001]_{mono}$ and $[001]_{ortho}$ zone axes, respectively. In (c) the Te and Ni are shown using gold and silver spheres, respectively. In (c) pure Te atomic columns are indicated by red arrows and Ni–Te atomic columns by yellow arrows. (e) HAADF-STEM image of monoclinic Ni_3Te_2 whose $(200)_{mono}$ planes show a modulation in intensity. (f) Simulated HAADF-STEM of monoclinic Ni_3Te_2 along the $[001]_{mono}$ zone axis confirming the modulation in intensity in the pure Te atomic columns indicated by white arrows. The Ni–Te columns are indicated by yellow arrows. (g) HAADF-STEM image showing a smooth transition from monoclinic Ni_3Te_2 with its modulated $(200)_{mono}$ planes (top) to orthorhombic $Ni_{2.88}Te_2$ with no modulation in $(200)_{ortho}$ planes (bottom).

$Ni_{2.88}Te_2$ are shown in Fig. 5a and b, respectively. It is apparent that some grains comprise a mix of orthorhombic $Ni_{2.88}Te_2$ and monoclinic Ni_3Te_2 phases. Moreover, within each phase, discrete orientation domains with specific misorientation angle/axes relationships remain (Fig. 5c - e). In Fig. 5c, these special boundaries correspond to 90°[001] (blue) and 90°[001] (red) for orthorhombic $Ni_{2.88}Te_2$ and monoclinic Ni_3Te_2, respectively. It follows that the 180°[001] (purple) and 180°[100] (teal) boundaries in monoclinic Ni_3Te_2 (Fig. 2c and d) are pseudo-symmetric boundaries that are largely eliminated when the map is re-indexed using both orthorhombic and monoclinic phases simultaneously. The lack of low-angle boundaries within each phase also means that the equivalent circle diameter of subgrains and grains of orthorhombic $Ni_{2.88}Te_2$ and monoclinic Ni_3Te_2 are similar at ~0.62 ± 0.32 μm and ~0.66 ± 0.51 μm, respectively.

Fig. 6a and b are a map plot and histogram, respectively, of the interphase boundary misorientation between orthorhombic $Ni_{2.88}Te_2$ and monoclinic Ni_3Te_2. It is apparent that the interphase boundaries tend to be misoriented at very low (0°–2°) or high (~90°) angles. This is ascribed to the orthorhombic $Ni_{2.88}Te_2$ and monoclinic Ni_3Te_2 phases sharing two previously unknown orientation relationships between them.

Orientation relationship 1 (OR1, left in Fig. 6b) is $(010)_{ortho} \parallel (010)_{mono}$, $[001]_{ortho} \parallel [001]_{mono}$ with an ideal misorientation angle

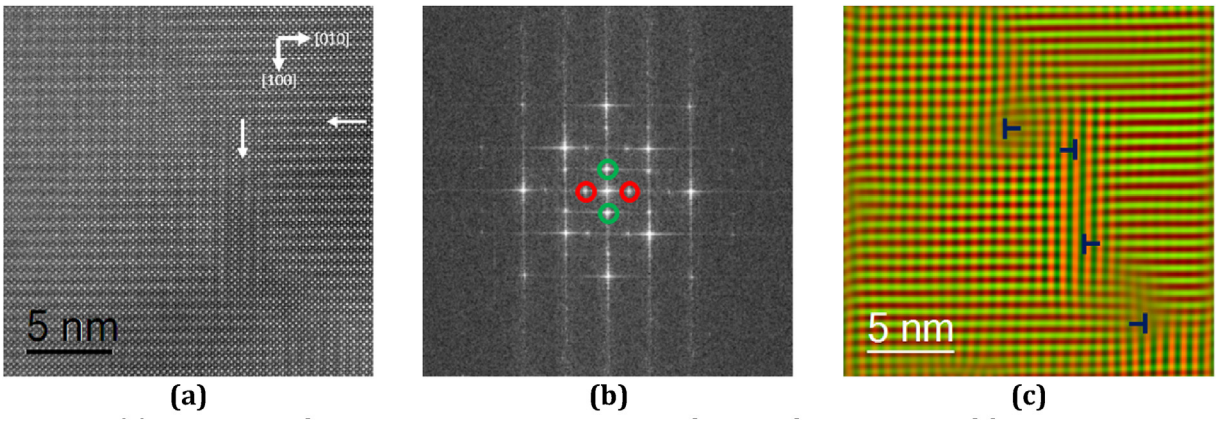

Fig. 8. (a) Atomic resolution HAADF-STEM image confirming the existence of discrete orientation domains within individual monoclinic Ni_3Te_2 grains. In (a) Ni vacancies (indicated by white arrows) are present along the $(200)_{mono}$ planes of the two domains. (b) Fast Fourier transformation of (a) showing reflections corresponding to the $(200)_{mono}$ planes of the two domains within the red and green circles. (c) RGB image formed by masking the $(200)_{mono}$ planes of the two domains and overlapping both resultant images. In (c), "dislocations" of the Ni-vacant planes are marked by blue T-shapes.

of 1.16° and ideal axes $[010]_{ortho}$ || $[010]_{mono}$. Orientation relationship 2 (OR2, right in Fig. 6b) is $(010)_{ortho}$ || $(100)_{mono}$, $[001]_{ortho}$ || $[001]_{mono}$ with an ideal misorientation angle of 90.0059° and ideal axes $[001]_{ortho}$ || $[001]_{mono}$.

It should be noted that the lattice parameters of monoclinic Ni_3Te_2 and orthorhombic $Ni_{2.88}Te_2$ are very similar (Tables 1 and 3); such that the main difference between the two phases is the lattice angle $\beta = 91.159°$ in monoclinic Ni_3Te_2. The latter could be a source of strain within individual grains comprising both phases; as seen in the low-angle boundary population in Fig. 6b and the first orientation relationship (OR1) with its very low 1.16° ideal misorientation angle when $(010)_{ortho}$ || $(010)_{mono}$.

Since the discrete orientation domains with specific misorientation angle/axes relationships in Fig. 5 may be misconstrued as pseudo-symmetry artefacts [14] and the very low misorientation angle of OR1 suggests an approximately smooth transition between orthorhombic $Ni_{2.88}Te_2$ and monoclinic Ni_3Te_2 phase, we employed aberration-corrected STEM to confirm the phases in the interfacial nickel telluride layer and the findings from EBSD analysis.

Fig. 7a is a selected area diffraction pattern of a monoclinic Ni_3Te_2 grain along the $[001]_{mono}$ zone axis. The strong and weak reflections belong to two monoclinic domains present in the same area from where the diffraction pattern was collected and are denoted by red and green arrows. It should be noted that along the common $[001]_{mono}$ zone axis of the two monoclinic domains, their $[100]_{mono}$ and $[010]_{mono}$ directions are 90° away from each other. This corresponds to the 90°[001] special boundaries shown in the EBSD maps (Fig. 5c and e).

Fig. 7b is an atomic resolution HAADF image where most planes have a modulation (*i.e.*- a variation) in intensity. However, in the region in-between the white lines at the bottom right-hand side of the image, the planes record no modulation in intensity. Since HAADF images are sensitive to the mean atomic number, the modulation in the intensity of the planes is indicative of a difference in chemical composition. The modulation is only present in monoclinic Ni_3Te_2 due to the ordered Ni vacancies in $(200)_{mono}$ planes. As shown in Fig. 7c, when visualising a $2 \times 2 \times 7$ supercell of monoclinic Ni_3Te_2 along the $[001]_{mono}$ zone axis, pure Te atomic columns (red arrows) and Ni—Te atomic columns (yellow arrows) are noted. In contrast, such vacancies are absent in orthorhombic $Ni_{2.88}Te_2$ (Fig. 7d). Therefore, the atomic resolution HAADF-STEM image in Fig. 7b comprises a mix of predominantly monoclinic Ni_3Te_2 and a smaller region, in-between the white lines at the bottom right-hand side of the image, of orthorhombic $Ni_{2.88}Te_2$.

Fig. 7e is an atomic resolution HAADF image of monoclinic Ni_3Te_2 whose $(200)_{mono}$ planes show a modulation in intensity. This modulation in monoclinic Ni_3Te_2 is confirmed by the HAADF image simulation in Fig. 7f; where $(200)_{mono}$ planes with similarly varying intensities are observed. Here, the white arrows indicate pure Te atomic columns (or conversely, Ni vacancies) while the yellow arrows indicate Ni—Te atomic columns. Fig. 7g is a HAADF-STEM image showing a smooth transition from monoclinic Ni_3Te_2 with its modulated $(200)_{mono}$ planes (top) to orthorhombic $Ni_{2.88}Te_2$ with no modulation in $(200)_{ortho}$ planes (bottom).

Fig. 8a shows an atomic resolution HAADF-STEM image along the $[001]_{mono}$ zone axis; confirming the existence of discrete orientation domains within individual monoclinic Ni_3Te_2 grains. It is evident that the Ni vacancies (indicated by white arrows) are present along the $(200)_{mono}$ planes of the two domains. The fast Fourier transformation of Fig. 8a further confirms the $[001]_{mono}$ zone axis and shows reflections corresponding to the $(200)_{mono}$ planes of the two domains within the red and green circles. Similar to the diffraction pattern in Fig. 7a, the red and green circles of the two monoclinic domains are 90° rotated away from each other around the $[001]_{mono}$ zone axis.

Masking the image in Fig. 8b, by selecting reflections corresponding to the $(200)_{mono}$ planes of the two domains within the red and green circles and overlapping both resultant images forms the RGB image in Fig. 8c. The latter shows an overlap of the $(200)_{mono}$ planes of the two domains; evidencing three distinct regions comprising vertical red lines (middle), horizontal green lines (right-hand side) and a criss-cross of vertical red and horizontal green lines (left-hand side). The RGB image also shows dislocations marked by blue T-shapes in regions where the two domains intersect each other. Here dislocations point to a shift in planes with Ni vacancies in the green domain by half a unit cell.

Figs. 7g and 8c confirm that: (i) distinct orthorhombic $Ni_{2.88}Te_2$ and monoclinic Ni_3Te_2 phases exist within individual grains comprising the interfacial nickel telluride layer. (ii) There is a smooth transition between orthorhombic $Ni_{2.88}Te_2$ and monoclinic Ni_3Te_2. (iii) There are distinct orientation domains in monoclinic Ni_3Te_2.

The three STEM-based conclusions corroborate the EBSD findings detailed above and are similar to the findings of Ref. [6]. The latter study quenched nickel telluride to room temperature and suggested that the interfacial nickel telluride layer comprises a mix of monoclinic Ni_3Te_2 and orthorhombic $Ni_{2.88}Te_2$. The existence of both phases is directly attributed to the peculiarities of the SPS fabrication technique itself [14]. Since the electron transfer

thorough the nickel telluride layer is expectedly dependant on the phase and crystallographic orientation of individual grains making up the interfacial layer, better control of the final state of this layer may lead to further improvements in the design, fabrication and overall efficiency of future thermoelectric devices.

4. Conclusions

A combination of EBSD and aberration-corrected HAADF-STEM was applied to comprehensively identify the phases in the interfacial nickel telluride layer formed at Ni electrode - PbTe thermoelectric material interfaces. The interfacial nickel telluride layer comprises a mix of room temperature, monoclinic Ni_3Te_2 coexisting with the transition $Ni_{2.88}Te_2$ orthorhombic phase. This is attributed to the rapid SPS fabrication technique used to form the interfacial layer. EBSD boundary maps and histograms detail the special boundaries resulting in orientation domains within both phases throughout the interfacial nickel telluride layer. Both EBSD and STEM data at interphase boundaries demonstrate an approximately smooth transition from orthorhombic to monoclinic phase with almost no crystal defects due to the small differences in lattice parameters and the prevalence of one of two previously unknown orientation relationships between the phases. The special boundaries resulting in discrete orientation domains within both phases throughout the interfacial nickel telluride layer needs to be considered when fabricating future thermoelectric devices.

Data availability

The raw/processed data required to reproduce these findings cannot be shared at this time due to technical or time limitations.

CRediT authorship contribution statement

Xavier Reales Ferreres: Data curation, Investigation, Writing - original draft. **Gilberto Casillas:** Formal analysis, Validation, Visualization, Writing - review & editing. **Sima Aminorroaya-Yamini:** Funding acquisition, Project administration. **Azdiar A. Gazder:** Conceptualization, Formal analysis, Methodology, Software, Supervision, Writing - review & editing.

Acknowledgments

The authors are grateful to Dr. Mitchell Nancarrow, University of Wollongong, Australia for assistance with sample preparation. This work was supported by an Australian Research Council (ARC) Linkage grant LP120200289, an ARC Discovery Early Career Award DE130100310, the AutoCRC Project Agreement 1-203 and the 2019 AIIM for GOLD (Investigator) grant schemes. The JEOL JSM-7001F FEG-SEM, the FEI Helios Nanolab G3 CX FIB-SEM and the JEOL JEM-ARM200F were funded by ARC Linkage Infrastructure, Equipment and Facilities grants LE0882613, LE160100063 and LE120100104, respectively.

Appendix A. Supplementary data

Supplementary data to this article can be found online at https://doi.org/10.1016/j.matdes.2019.108252.

References

[1] H. Xia, et al., Bonding and interfacial reaction between Ni foil and n-type PbTe thermoelectric materials for thermoelectric module applications, J. Mater. Sci. 49 (4) (2014) 1716–1723.
[2] X. Reales Ferreres, et al., One-step bonding of Ni electrode to n-type PbTe–a step towards fabrication of thermoelectric generators, Mater. Des. 107 (2016) 90–97.
[3] J. Barstad, On the tellurides of nickel, Acta Chem. Scand. 20 (10) (1966) 2865–2879.
[4] T. Massalsky, Binary Alloy Phase Diagrams, Second Edit, ASM International, USA, 1990, pp. 940–942.
[5] K. Klepp, K. Komarek, Übergangsmetall-chalkogensysteme, 3. Mitt.: das system nickel-tellur, Monatshefte Chem./Chem. Mon. 103 (4) (1972) 934–946.
[6] R.B. Kok, G.A. Wiegers, F. Jellinek, *The system nickel-tellurium I. Structure and some superstructures of the $Ni_{3\pm q}Te_2$ phase (preliminary communication)*, Recl. Trav. Chim. Pays-Bas 84 (12) (1965) 1585–1588.
[7] Ball, R.G.J., et al., *Thermochemical Data Acquisition. Part II*. 1991, Commission of the European Communities.
[8] S.A. Forman, P.M.A., Am. Mineral. 34 (1949) 441–451.
[9] A.L.N. Stevels, Phase Transitions in Nickel and Copper Selenides and Tellurides, 1969.
[10] L.D. Landau, On the theory of phase transitions, Zh. Eksp. Teor. Fiz. 7 (19–32) (1937).
[11] R.A. Schwarzer, et al., Present state of electron backscatter diffraction and prospective developments. Electron Backscatter Diffraction in Materials Science, Springer, 2009, pp. 1–20.
[12] A.J. Wilkinson, P.B. Hirsch, Electron diffraction based techniques in scanning electron microscopy of bulk materials, Micron 28 (4) (1997) 279–308.
[13] D. Dingley, Progressive steps in the development of electron backscatter diffraction and orientation imaging microscopy, J. Microsc. 213 (3) (2004) 214–224.
[14] X.R. Ferreres, S. Aminorroaya Yamini, Rapid fabrication of diffusion barrier between metal electrode and thermoelectric materials using current-controlled spark plasma sintering technique, J. Mater. Res. Technol. 8 (1) (2019) 8–13.
[15] X.R. Ferreres, et al., Solid-state bonding of bulk PbTe to nickel electrode for thermoelectric modules, ACS Appl. Energy Mater. 1 (2) (2018) 348–354.
[16] R. Hielscher, H. Schaeben, A novel pole figure inversion method: specification of the MTEX algorithm, J. Appl. Crystallogr. 41 (6) (2008) 1024–1037.
[17] G. Nolze, R. Hielscher, Orientations - perfectly colored, J. Appl. Crystallogr. 49 (5) (2016) 1786–1802.
[18] L. Gulay, I. Olekseyuk, Crystal structures of the compounds Ni 3 Te 2, Ni 3–δ Te 2 (δ= 0.12) and Ni 1.29 Te, J. Alloy. Comp. 376 (1) (2004) 131–138.